remote sensing

MDPI

Article

Impact of Aerosol Mixing State and Hygroscopicity on the Lidar Ratio

Zhijie Zhang [1,2,3,†], Li Liu [2,†], Baomin Wang [1,3,4,*], Haobo Tan [2], Changxing Lan [1,5], Ye Wang [1,3] and Pakwai Chan [6]

1 Guangdong Provincial Key Laboratory for Climate Change and Natural Disaster Studies, School of Atmospheric Sciences, Sun Yat-sen University, Zhuhai 519082, China; zhzhij33@mail2.sysu.edu.cn (Z.Z.); changxing.lan@wsu.edu (C.L.); wangy393@mail2.sysu.edu.cn (Y.W.)
2 Institute of Tropical and Marine Meteorology of CMA, Guangzhou 510640, China; liul@gd121.cn (L.L.); hbtan@gd121.cn (H.T.)
3 Southern Marine Science and Engineering Guangdong Laboratory (Zhuhai), Zhuhai 519082, China
4 Guangdong Provincial Field Observation and Research Station for Climate Environment and Air Quality Change in the Pearl River Estuary, Guangzhou 510275, China
5 Laboratory for Atmospheric Research, Department of Civil and Environmental Engineering, Washington State University, Pullman, WA 99164, USA
6 Hong Kong Observatory, Kowloon, Hong Kong; pwchan@hko.gov.hk
* Correspondence: wangbm@mail.sysu.edu.cn
† These authors contributed equally to this work.

Abstract: The lidar ratio (*LR*) is a key parameter for the retrieval of atmospheric optical parameters from lidar equations. In this study, we simulated the optical parameters to investigate the impact factors of the *LR* using a three-component optical aerosol assumption based on the Mie model. The simulated *LR* was generally related to the overall particle size of the aerosols, the proportion of elemental carbon (EC), as well as aerosol mixing states and hygroscopicity. The *LR* was positively correlated with the particle size and volume fraction of elemental carbon (f_{EC}). The *LR* increased more than three-fold with the increase in f_{EC} from 0% to 40%. The *LR* of the core-shell (CS) mixing state and homogeneously internal (INT) mixing state was greater than that of the external (EXT) mixing state. The *LR* of all mixing states increased monotonically with hygroscopicity when the f_{EC} was below 10%, while the *LR* of the core-shell mixing state (homogeneously internal mixing state) initially decreased (increased) and then increased (decreased) with increasing hygroscopicity when the f_{EC} was more than 20%. These results will help in selecting a reasonable *LR* for practical applications.

Keywords: lidar ratio; mixing state; hygroscopic growth; Mie model

Citation: Zhang, Z.; Liu, L.; Wang, B.; Tan, H.; Lan, C.; Wang, Y.; Chan, P. Impact of Aerosol Mixing State and Hygroscopicity on the Lidar Ratio. *Remote Sens.* **2022**, *14*, 1554. https://doi.org/10.3390/rs14071554

Academic Editor: Simone Lolli

Received: 11 February 2022
Accepted: 21 March 2022
Published: 23 March 2022

1. Introduction

Atmospheric aerosol particles have a significant direct effect on the radiative balance (IPCC, 2013) and can weaken the hydrological cycle [1]. As cloud condensation and ice nuclei, aerosols play an important role in affecting the cloud characteristics, changing the life cycle of clouds, and thus impacting precipitation [2,3]. Atmospheric aerosol observation methods primarily include ground-based observations and remote sensing detection. Elastic backscatter lidar is one of the most widely used remote sensing detection methods, which can observe the microphysical aerosol characteristics and their vertical distributions. A key parameter, referred to as the lidar ratio (*LR*), is typically introduced to retrieve the lidar signal and obtain the vertical distribution characteristics of the aerosol extinction coefficient when solving the lidar equation [4,5]. Previous studies have indicated that the *LR* can be directly observed by a combined Raman elastic-backscatter lidar [6–8] or accurately retrieved by a high spectral resolution lidar [9,10]. The *LR* was also retrieved by combining multi-wavelength lidar, a sunphotometer, and other ground-based observation instruments, according to previous research [11–14]. However, the physical and chemical properties of

aerosols have great heterogeneity and uncertainty in temporal and spatial distributions; hence, it is essential to study how and why the *LR* changes due to these factors.

The traditional method to determine the *LR* in practical studies is by employing empirical constants with respect to the types of aerosols, which might lead to great uncertainty. For instance, Schuster et al. [15] compared lidar products from Cloud-Aerosol Lidar, Infrared Satellite Observation (CALIPSO), and Aerosol Robotic Network (AERONET), indicating that the *LR* of dust aerosols (40 sr) calculated by CALIPSO is smaller than that calculated by AERONET (49.7 sr). AERONET and CALIPSO's algorithm used to calculate the optical and microphysical properties have been improved in recent years. Shin et al. [16] studied the *LR* of mixed dust using the version three data released by AERONET, and proved that the *LR* of the mixture of fine-mode particles with dust is higher than that of the pure dust aerosol. Kim et al. [17] optimized CALIPSO's aerosol classification algorithm by submitting some new aerosol types. Error analysis by He et al. [13] suggested that the *LR* is the main error source in the retrieval processes of lidar. Shimizu et al. [18] indicated that using a constant *LR* value of 50 sr in strong dust events resulted in an error of extinction coefficient up to 50%. Different values of *LR* will contribute to a great impact on the properties of PBL aerosol products of lidar. Zhao et al. [19] calculated the lidar ratio under different relative humidity and compared the extinction coefficient profiles retrieved by different *LR*. The results show that fixed *LR* may lead to deviation of lidar products such as the mixed layer height and the radiation energy distribution in the vertical direction. The characteristics of the extinction coefficient calculated by corrected *LR* may also contribute to a reinterpretation of the structure of the mixed layer.

The *LR* is determined by the extinction and backscattering coefficients (Equation (1)). These two aerosol optical parameters are jointly influenced by several factors, such as the aerosol particle number size distribution (PNSD), the mixing state of elemental carbon (EC), hygroscopicity, relative humidity (*RH*), complex refractive index, and incident light wavelength. Zhao et al. [20] calculated the *LR* at different wavelengths using Mie theory and the PSND of aerosols measured by an aerodynamic particle sizer spectrometer (APS). The results suggested that the *LR* is positively correlated with the effective radius of the aerosol and the ratio of coarse and fine particles. Song et al. [21] found that the *LR* has a high correlation with the Ångström exponent, which is typically used to indicate the overall particle size of aerosols, when the aerosol types are continental, marine, and desert aerosols.

The mixing state of EC refers to the pattern of how the EC is mixed with a non-light absorbing component, including the external mixing state (EXT), core-shell mixing state (CS), and homogeneously internal mixing state (INT). The optical properties of aerosols vary substantially with the mixing states [22–24]. Numerical simulations suggest that the absorption coefficient of aerosols in the INT can reach 2–3 times of that in the EXT [25–27]. Additionally, the difference in the hemispherical backscattering fraction (HBF) between the EXT and the CS was greater than 50% at an incident light wavelength of 550 nm [28]. However, few studies have analyzed the influence of the aerosol mixing state on the *LR*, which is one of the main objectives of this study. There are significant diurnal variation characteristics and regional distinctions in the different mixing states [28–30], which complicates the analysis and applications of the *LR*.

The optical properties of aerosols are also affected by hygroscopicity, which is typically expressed by the growth factor (*Gf*) and hygroscopic enhancement factor of aerosol optical properties ($f(RH)$). The variations in extinction and backscattering are not obvious under relatively low *RH*, while the extinction and scattering of aerosols increase exponentially with increasing *RH* [31–33]. Aerosols from different sources respond differently to the *LR* with an increase in the ambient *RH* [34]. Radiosonde data revealed that the *RH* exhibited obvious profile characteristics with increasing height, particularly within the mixing layer [35,36]. Zhao et al. [20] analyzed the influence of the particle number size distribution, hygroscopicity, and *RH* profile on the *LR*. When the *RH* was 92%, the *LR* value was 2.2 times that under dry conditions. Both the observation and simulation results revealed that using a constant *LR* in the retrieval of lidar data may result in a large error in

the retrieved aerosol extinction profile if the influence of the aerosol hygroscopicity and *RH* on the *LR* is not considered.

As stated above, many factors affect the *LR* value of aerosol. However, an inaccurate *LR* value will result in the deviation of the lidar inversion products. Accurate *LR*, which is obtained by comparing different channels of Raman lidar [37] or constraining the aerosol optical depths (AODs) [38], will improve the accuracy of lidar products such as atmospheric boundary layer height, optical thickness, extinction coefficient profile, backscattering coefficient profile, and cloud height.

Therefore, it is essential to conduct a detailed study on the factors influencing the *LR* variation to improve the accuracy of lidar data retrieval. In this study, PNSD data of the different types of aerosol were selected as the samples to calculate the theoretical *LR* value based on the 'three-component optical equilibrium aerosol model' [39]. The results of the *LR* are varied with the PNSD, f_{EC}, mixing state, hygroscopicity, and *RH*. The remainder of this paper is organized as follows: Section 2 introduces the *LR* calculation methods. The results are described in Section 3, and the conclusions are discussed in Section 4.

2. Methodology

2.1. Calculation of Lidar Ratio in the Dry Condition

The *LR* refers to the ratio of the extinction coefficient to the backscattering coefficient (Equation (1)).

$$LR = \frac{\alpha}{\beta} \tag{1}$$

where α is the extinction coefficient of aerosols and β is the 180° backscattering coefficient of aerosol, which are defined in Equations (2) and (3), respectively:

$$\alpha = \int \pi r^2 Q_{ep}(r, \lambda, \widetilde{m}) n(r) dr \tag{2}$$

$$\beta = \int \pi r^2 Q_{bac}(r, \lambda, \widetilde{m}) n(r) dr \tag{3}$$

where r is the radius of a single particle; λ is the wavelength of the incident laser; $\widetilde{m}$ is the complex refractive index of the particles; $n(r)$ is the PNSD; and Q_{ep} and Q_{bac} are the extinction and backscattering efficiencies of the particles, respectively. Therefore, the theoretical value of the *LR* is calculated using Equation (4):

$$LR = \frac{\int \pi r^2 Q_{ep}(r, \lambda, \widetilde{m}) n(r) dr}{\int \pi r^2 Q_{bac}(r, \lambda, \widetilde{m}) n(r) dr} \tag{4}$$

Generally, the PNSD is simplified as a lognormal distribution model and can be expressed as follows:

$$n(r) = \frac{dN}{dr} = \sum_{i=1}^{M} \frac{N_{tot,i}}{\sqrt{2\pi} r ln\sigma_{0,i}} exp\left(-\frac{(lnr - lnr_{0,i})^2}{2(ln\sigma_0)^2} \right) \tag{5}$$

where $N_{tot,i}$ denotes the total number concentration of mode i, $\sigma_{0,I}$ and $r_{0,i}$ are the standard deviation and median radius of mode i, respectively. The number of modes introduced by M includes the nucleation mode (0–20 nm), Aitken mode (20–100 nm), and accumulation mode (100–2000 nm). In this study, the extinction efficiency and 180° backscattering efficiency are calculated using two aerosol simplified spherical models based on the Mie theory: homogeneously spherical model (BHMie) and core-shell double-layer spherical model (BHCoat). In order to simplify the model, the wavelength of the lidar selected in this study is 532 nm.

Aerosols are divided into three components based on their optical characteristics: the light-absorbing component (i.e., EC), non-light-absorbing component (NLB), and water (which is not included in the dry aerosol particles) [22,23,40]. The optical parameters

depend on the complex refractive index of each component and the aerosol mixing state when the aerosol PNSD is known. Instead of choosing specific types of aerosol, this study modifies the overall complex refractive index of aerosol by changing the fractions of the three components and their mixing states.

In this work, the complex refractive indices of the EC component ($\widetilde{m}_{\mathrm{EC}} = 1.8 + 0.55i$), NLB component ($\widetilde{m}_{\mathrm{NLB,dry}} = 1.55 + 10^{-7}i$), and water ($\widetilde{m}_{\mathrm{water}} = 1.33 + 10^{-9}i$) were obtained from previous studies [28,41–45]. The volume fraction of EC (f_{EC}), which is defined in Equation (6), was assumed to be uniform for each particle size in this study.

$$f_{\mathrm{EC}} = \frac{V_{\mathrm{EC}}}{V_{\mathrm{dry}}} \tag{6}$$

Therefore, the aerosol complex refractive index of homogeneously internal mixture is calculated according to the volume averaging rule [46]:

$$\widetilde{m}_{\mathrm{INT,dry}} = \widetilde{m}_{\mathrm{EC}} f_{\mathrm{EC,dry}} + \widetilde{m}_{\mathrm{NLB,dry}} (1 - f_{\mathrm{EC,dry}}) \tag{7}$$

2.2. Calculation of Lidar Ratio under the Wet Condition

The aerosol particle diameter, complex refraction index, optical properties, and *LR* change when hygroscopic particles absorb moisture under wet conditions. The hygroscopic growth factor (*Gf*) is introduced to describe the increase in particle size:

$$Gf = \frac{r_{\mathrm{wet}}}{r_{\mathrm{dry}}} \tag{8}$$

The PNSD under wet conditions is calculated using the *Gf* and PNSD under dry conditions. The hygroscopic growth of aerosol particles is affected by the hygroscopicity and *RH*. Aerosol hygroscopicity can be expressed by parameter κ [47], which has been reported to range from 0–0.6 in the majority of regions in China [48]. The hygroscopic growth factor of aerosol particles is calculated as in previous studies [49]:

$$Gf \cong \left(1 + \kappa \frac{RH}{100 - RH}\right)^{\frac{1}{3}} \tag{9}$$

The extinction and backscattering efficiencies of particles that have undergone hygroscopic growth are solved using three spherical particle models. The necessary input parameters are listed in Table 1.

Table 1. Input parameters and the applied Mie model for the three mixing states under dry and wet conditions.

Mixing State	Applied Mie Model	Input Parameter	
		Dry Condition	Wet Condition
EXT	BHMie	$r_t, \lambda, \widetilde{m}_{\mathrm{EC}}, \widetilde{m}_{\mathrm{NLB,dry}}$	$r_t Gf, \lambda, \widetilde{m}_{\mathrm{EC}}, \widetilde{m}_{\mathrm{NLB,wet}}$
CS	BHCoat	$r_t, r_c, \lambda, \widetilde{m}_c, \widetilde{m}_s$	$r_t Gf, r_c, \lambda, \widetilde{m}_c, \widetilde{m}_s$
INT	BHMie	$r_t, \lambda, \widetilde{m}_{\mathrm{INT,dry}}$	$r_t Gf, \lambda, \widetilde{m}_{\mathrm{INT,wet}}$

Where $r_t, \lambda, \widetilde{m}_{\mathrm{EC}}, \widetilde{m}_{\mathrm{NLB,dry}}, \widetilde{m}_{\mathrm{NLB,wet}}, r_c, \widetilde{m}_c, \widetilde{m}_s, \widetilde{m}_{\mathrm{INT,dry}}$, *and* $\widetilde{m}_{\mathrm{INT,wet}}$ represent the radius of the particle, incident wavelength, complex refractive index of the EC component, complex refractive index of the NLB component under dry conditions, complex refractive index of the NLB component under dry conditions, radius of the core, complex refractive index of the core, complex refractive index of the shell, overall complex refractive index of the homogeneously internal mixture particles under dry conditions, and overall complex refractive index of the homogeneously internal mixture particles under wet conditions, respectively.

We also assumed that *Gf* is uniform for all aerosol particle sizes and that the EC component is water-insoluble, implying that $\widetilde{m}_{EC}$ does not change at all. The complex refractive indices under wet conditions were calculated as follows:

$$\widetilde{m}_{NLB,wet} = \frac{\widetilde{m}_{NLB,dry} f_{NLB,wet} + \widetilde{m}_{water} f_{water}}{f_{NLB,wet} + f_{water}} \quad (10)$$

$$\widetilde{m}_{INT,wet} = \widetilde{m}_{EC} f_{EC,wet} + \widetilde{m}_{NLB,dry} f_{NLB,wet} + \widetilde{m}_{water} f_{water} \quad (11)$$

where $f_{NLB,wet}$, $f_{EC,wet}$, and f_{water} represent the volume ratio of the NLB component, EC component, and water in the wet condition, respectively (Equations (12)–(14)):

$$f_{EC,wet} = \frac{f_{EC}}{f_{EC} + (1 - f_{EC})(Gf)^3} \quad (12)$$

$$f_{NLB,wet} = \frac{1 - f_{EC}}{f_{EC} + (1 - f_{EC})(Gf)^3} \quad (13)$$

$$f_{water} = 1 - f_{EC,wet} - f_{NLB,wet} \quad (14)$$

3. Results and Discussion

3.1. Influence of the Particle Number Size Distribution on the LR

To inform the *LR* characteristics among the different regions, the aerosol PNSDs of East Asia (EA), Europe (EU), Latin America (LA), and North America (NA), reported by Wu et al. [50]), were utilized to simulate the aerosol optical properties as well as the *LR*. The median PNSDs of the four regions were obtained by synthesizing 525 PNSD observations from 1998 to 2017, as shown in Figure 1. The PNSDs exhibited significant variations in their shapes and magnitudes. The aerosol number concentration in EA is approximately the same order of magnitude as that in NA, while the diameter corresponding to the prominent mode in EA (60 nm) is approximately twice as large as that in LA (30 nm). The median PNSDs in EU and LA display similar structural characteristics, both of which are dominated by the nucleation mode and Aitken mode particles [50]. It can be seen from Figure 1 that the samples selected in this study are mainly fine-mode aerosol particles. Shin et al. [51] reported that dust was hydrophobic aerosol with coarse mode fraction over 0.9 and volume depolarization ratio greater than 0.2. Therefore, we do not consider the effect of dust in this study.

Based on the Mie theory, the *LR*s were simulated for the EXT, CS, and INT mixing states. The volume fraction of EC was set to 0.1, and the complex refractive indices were 1.8 + 0.55i and 1.55 + 10^{-7}i for EC and NLB, respectively (refer to Section 2). Considering the difference in the type of PNSD, the *LR* was noticeably lower in the NA region than in the other three regions by 30–50%, as shown in Figure 2. The median *LR* values in EA, EU, and LA were similar in magnitude under the same mixing conditions. The proportion of PNSD in the nucleation, Aitken, and accumulation modes shown in Figure 3 are used to study the influence of the number size distribution on *LR*.

The calculated *LR* value in this study was relatively larger than that obtained by Raman lidar in previous studies [6,37] wherein the average *LR* was 39 sr to 59 sr and 37 sr to 65 sr for urban haze and South-East Asian aerosols, respectively. In addition to the distinction of aerosol physical and chemical characters among regions, another probable reason is that the backscattering signal obtained by Raman lidar is not only the backscattering signal at 180°, but also that within a small angle at approximately 180°. This leads to a larger backscattering signal in the actual observation compared to the calculated theoretical backscattering value. On the other hand, the fraction of EC in mainland China was reported to be between 5% and 10% [52] while it was occasionally increased to approximately 30% in some pollution events [53–55]. Thus, considering that the *LR* rapidly increased with f_{EC} (discussed in Section 3.3), the EC content reported in previous observations were typically lower than the EC volume ratio assumed in this study.

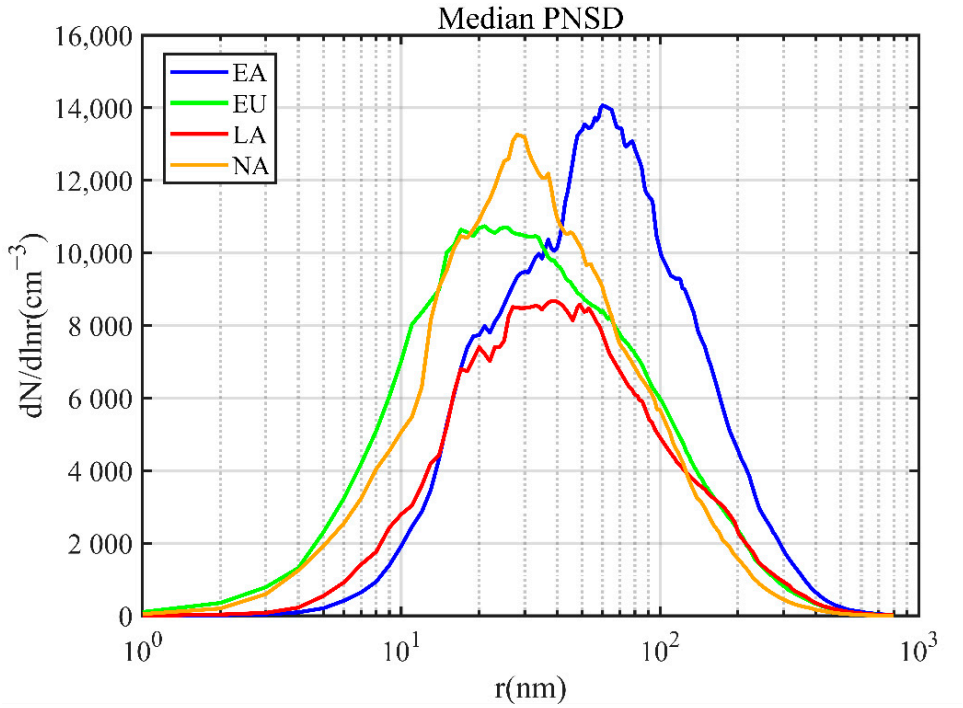

Figure 1. Representative PNSDs in different regions. The representative samples of the four regions in the figure are the median value of the PNSD.

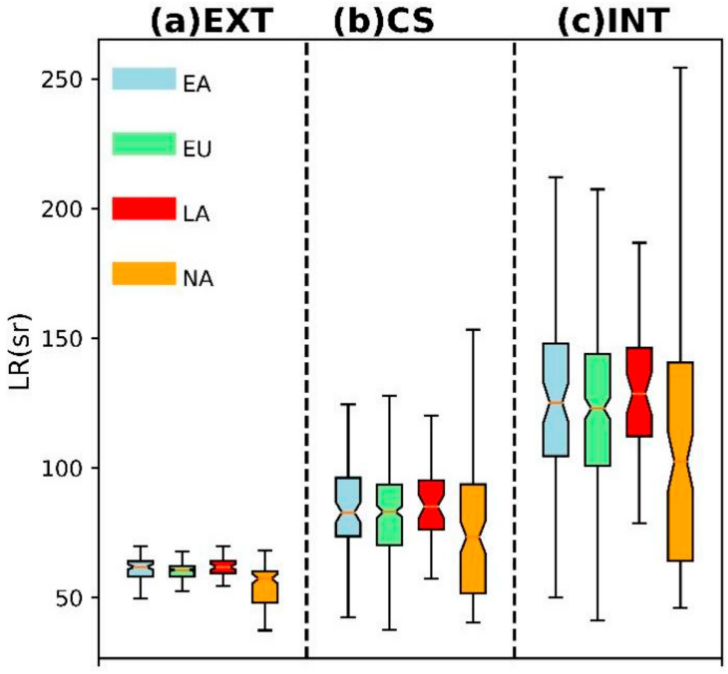

Figure 2. Values of the *LR* of all samples in different regions under the condition of f_{EC} = 0.1. EXT, CS, and INT represent the external, core-shell, and internal mixing states, respectively.

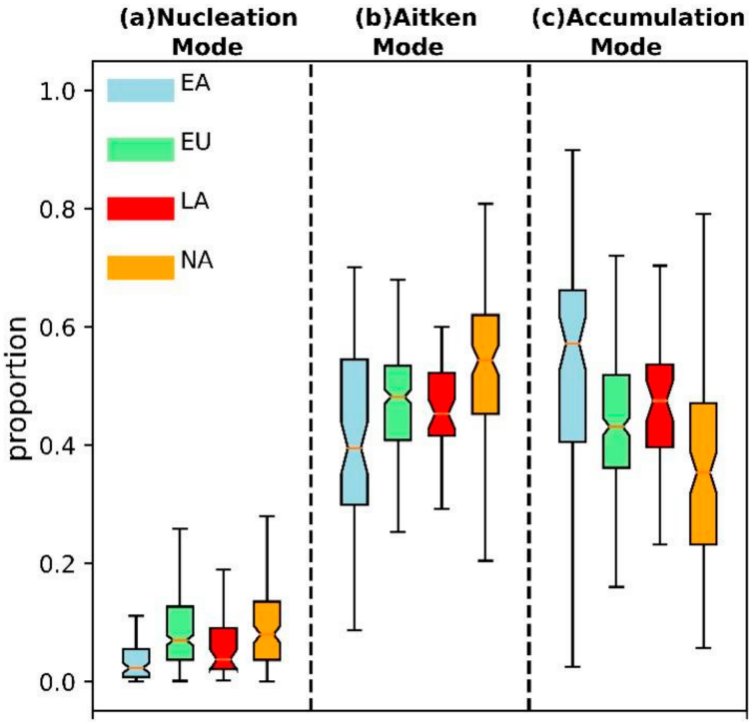

Figure 3. Proportion of the three modes of aerosol number concentration in the four regions. The proportion of (**a**) nucleation mode aerosols, (**b**) Aitken mode aerosols, and (**c**) accumulated modal aerosols.

Similarly, the proportions of the accumulation and Aitken modes were found to be the highest and the lowest, respectively, in the EA, while those in NA showed the opposite trends. This shows that the aerosol size particles in EA tend to be larger than those in LA. The proportions of both the accumulation and Aitken modes are high in EU and LA, corresponding to a wide range of PNSD peaks. To study the influence of particle size on the *LR*, the effective particle size $r_{\mathrm{eff,i}}$ is defined by Equation (15) [20,56]:

$$r_{eff,i} = \frac{\int \pi r^3 n_i(r) dr}{\int \pi r^2 n_i(r) dr} \tag{15}$$

where i represents the number of samples (up to 525), and n_i represents the number of particles of the corresponding particle size. The r parameter is used to indicate the overall particle size of the corresponding sample. A regression analysis of the *LR* was conducted for each sample, and the results are shown in Figure 4.

As shown in Figure 4, the r_{eff} values are generally positively correlated with the *LR* value for all mixing states, consistent with previous studies [14,20,21]. However, it is worth noting that, when the effective particle size increased higher than 380 nm, the *LR* of the EXT tended to be negatively correlated with the effective particle size. This is because the *LR* mainly depends on the variation of aerosol extinction and backscattering for different PNSD and mixing states. As shown in Figure S3, the variations of extinction and backscattering efficiency of single particles were displayed. The extinction efficiency of a single particle rapidly increases with the particle size, meanwhile, the backscattering efficiency keeps increasing with fluctuation. The fast increase in the extinction efficiency dominates the *LR* and leads to an increase in *LR*. However, when the particle size exceeds a critical point, the extinction efficiency decreases with the increase in particle size, as is shown in Figure S3a, while the backscattering efficiency still increases with fluctuation, as is shown in Figure S3b, which will lead to the decrease in *LR*. This demonstrated that the *LR* was positively correlated with r_{eff} in a certain effective particle size range, while the range is different for three mixing states.

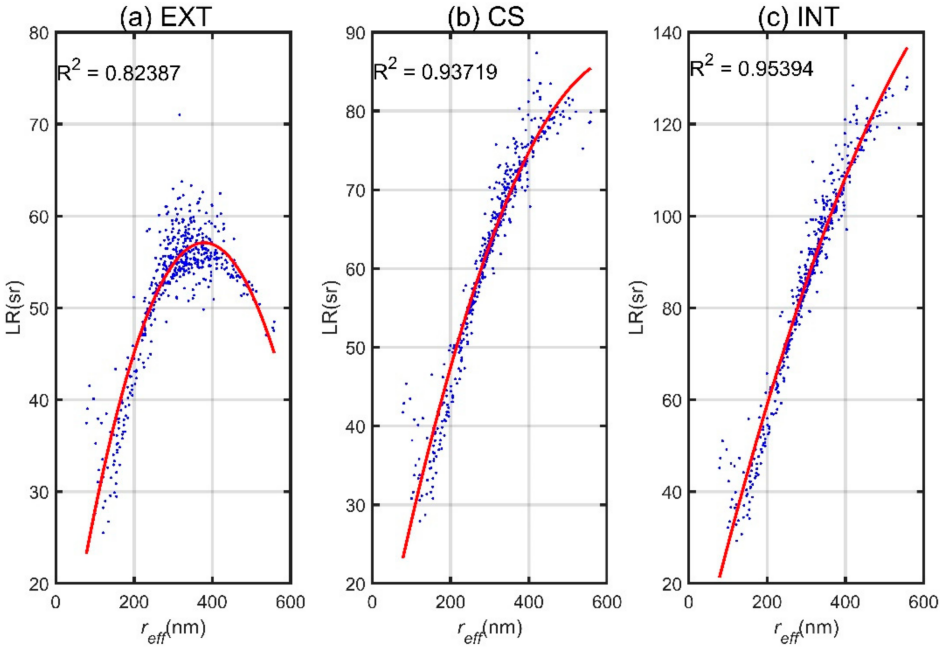

Figure 4. Regression analysis results of r_{eff} and *LR* for the (**a**) external mixing state, (**b**) core-shell mixing state, and (**c**) homogeneously internal mixing state.

3.2. Influence of the Mixing State on LR under the Dry Condition

As is shown in Figure 2, the *LR* of INT is the highest among the three mixing states, whereas that of the EXT is the lowest. For the same type of PNSD, there is little distinction among the extinction coefficients calculated for the three mixing states (Figure 5a), which agrees with the results of previous studies [28,29,39]. As is shown in Figure 5b, the simulated absorption coefficients of INT and CS were considerably higher than those of EXT. This is because only the EC particles contribute to the light absorption of aerosols in EXT. In contrast, in INT and CS, the light absorption capacity of particles is amplified when EC is mixed internally or as a core surrounded with non-EC components due to the 'lensing effect' [28,29,39]. Consequently, as is shown in Figure 5c, the simulated scattering coefficient of EXT is higher than that of CS and INT. At the same time, Figure 5d also shows that the backscattering coefficient of CS and INT is smaller than that of EXT. This illustrates that backscattering is affected by the aerosol mixing states, and thus alters the *LR*.

The median value and standard deviation of the *LR* exhibited significant differences under the different mixing states, as is shown in Figure 2. Under EXT, the *LR* shows the lowest median and the smallest standard deviation, whereas INT shows the highest median and the highest standard deviation. To evaluate the effects of different mixing states on the *LR* calculation, the ratios of *LR* under the three mixing states are defined in Equations (16) and (17).

$$r1 = \frac{LR_{\mathrm{CS},i}}{LR_{\mathrm{EXT},i}} \tag{16}$$

$$r2 = \frac{LR_{\mathrm{INT},i}}{LR_{\mathrm{EXT},i}} \tag{17}$$

where i represents the number of samples (up to 525), and $r1$ and $r2$ are the ratios of *LR* under CS and INT to those under EXT, respectively. In general, the median $r1$ and $r2$ values were 1.2–1.4 and 1.7–2.1, respectively (Figure 6). The variation range of $r2$ is greater than that of $r1$, which implies that the *LR* is most sensitive to INT. It is necessary to evaluate the influence of the EC mixing state on the *LR* calculation and improve the accuracy of the extinction coefficient in the retrieval of the lidar equation.

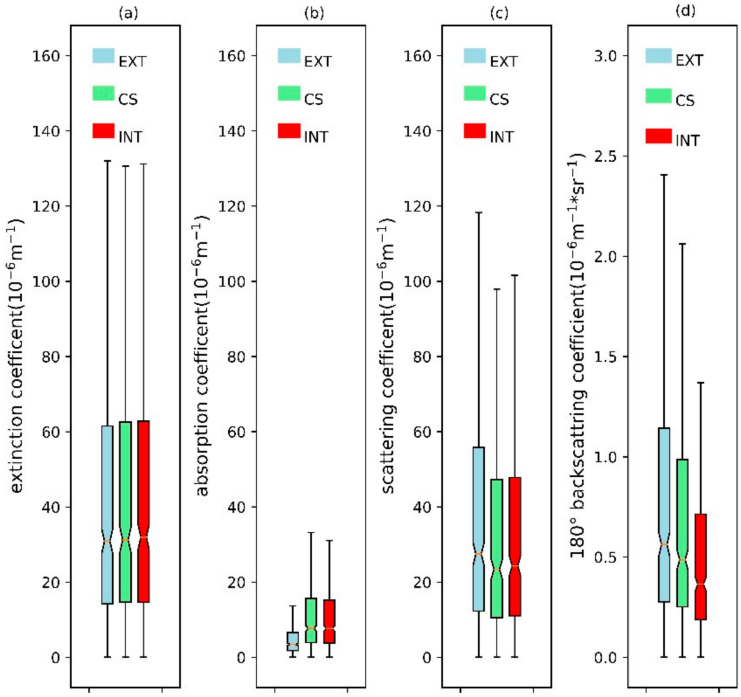

Figure 5. (**a**) Extinction coefficients, (**b**) absorption coefficients, (**c**) scattering coefficients, and (**d**) backscattering coefficients of aerosols under three mixing states.

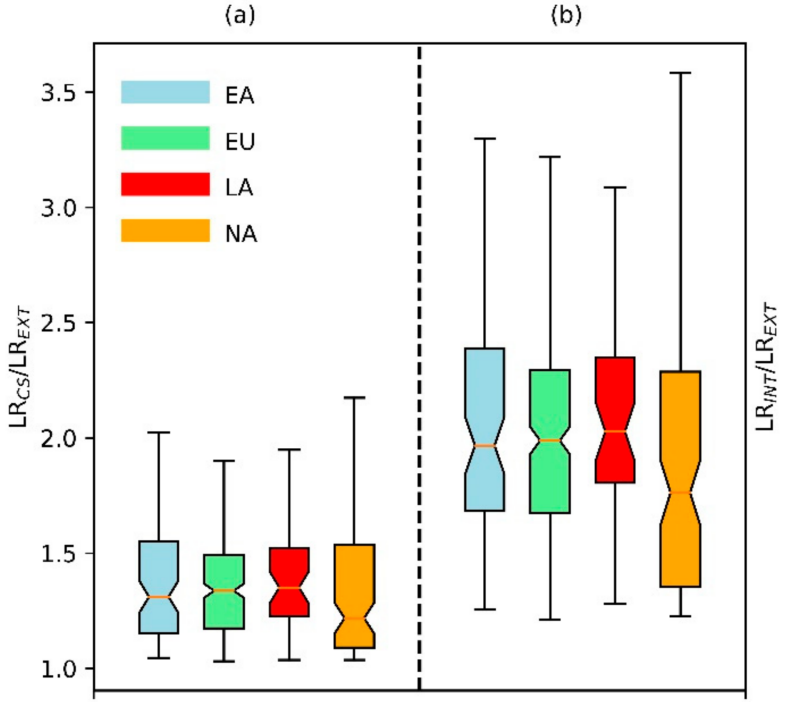

Figure 6. The ratio of the *LR* of (**a**) the core-shell mixing state to that of the external mixing state, (**b**) the homogeneously internal mixing state to that of the external mixing state.

3.3. Influence of the Volume Fraction of EC on the LR under the Dry Condition

The *LR* is also affected by the chemical composition, particularly the ratio of the EC volume to the total aerosol volume, apart from the PNSD and mixing states. The volume ratio of EC (f_{EC}) changes the aerosol complex refraction index, thus altering the *LR* calculated from the Mie model. To investigate the impact of the f_{EC} on the *LR* of different

mixing states, Figure 7 shows the change of simulated *LR* with f_{EC} values of EXT, CS, and INT.

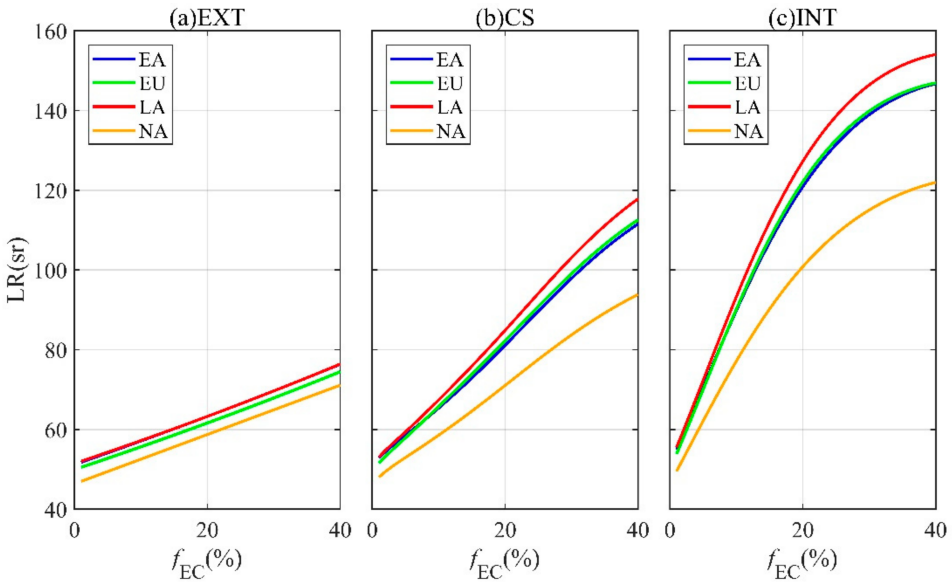

Figure 7. The *LR* changes with f_{EC} under PNSDs of different regions in (**a**) external mixing state, (**b**) core-shell mixing state, and (**c**) homogeneously internal mixing state.

The medians of the PNSDs in the EA, EU, LA, and NA regions were chosen for the calculation (Figure 1) (Figure S1, hygroscopic parameters). In general, the *LR* values in the four regions increased with increasing f_{EC} when the f_{EC} was less than 40%. However, the growth rates of *LR*s were different under the three mixing states. The *LR* was the highest in LA and the lowest in NA due to the differences in PNSDs, which was consistent with the results shown in Figure 1. As shown in Figure 7a, the *LR* increased linearly with an increase in the f_{EC} under EXT. A higher f_{EC} implies the presence of more EC particles, which can linearly enhance the aerosol absorption coefficient due to the increase in independent light-absorbing EC particles. Nevertheless, as f_{EC} increased, the *LR* values nonlinearly increased under CS and INT (Figure 7b,c). With an increase in the volume fraction of EC, the EC core in each particle became greater under CS, which led to a stronger 'lensing effect'. Similarly, the light-absorbing ability of aerosols increased, owing to the change in the aerosol complex index under INT, which also nonlinearly enhanced the light absorption and the *LR*. Moreover, the discrepancy in the *LR* between the LA and NA regions increased, particularly for INT. The results indicated that *LR* increased with an elevated volume fraction of EC, whereas the growth rate of *LR* was different under the three mixing states. Moreover, the discrepancy in the *LR* calculated with different PNSDs barely changed under EXT. The discrepancy of *LR* increased with increasing f_{EC} under CS and INT, and both the PNSD and f_{EC} impacted the 'lensing effect', thereby altering the *LR*.

3.4. Influence of Hygroscopicity on the LR

The hygroscopic growth of aerosol particles is affected by the hygroscopicity and *RH*. In this section, the median value of PNSD in mainland China [50] is used to calculate the aerosol optical properties and the *LR* based on the Mie model. We used single hygroscopicity parameter (κ = 0.0–0.6) data from hygroscopic experiments in China over the past 20 years [48] to study the impact of hygroscopicity on the *LR*. The growth factor (Gf) of particle size was obtained by combining κ and *RH* according to Equation (9) (Brock et al. [49]), and was then utilized into the Mie model calculation in wet condition, the details of which were given in Section 2.2 (Figure S2).

To study the variation in the *LR* due to the hygroscopic growth of aerosol particles, the hygroscopic enhancement factor of *LR* was introduced in Equation (18). The variations in *LR* with κ, *RH*, and f_{EC} for the three mixing states are shown in Figure 8.

$$f(RH)_{LR} = \frac{LR_{\mathrm{wet}}}{LR_{\mathrm{dry}}} \tag{18}$$

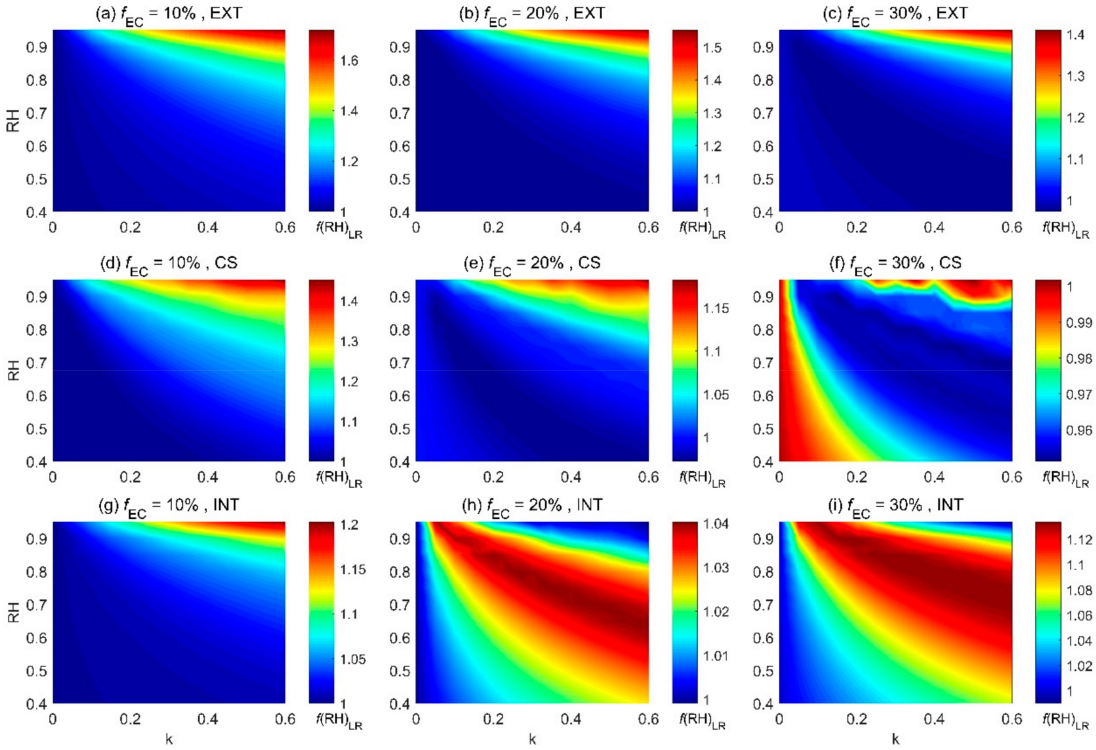

Figure 8. The *LR* under different κ and f_{EC} values. The X axis represents κ, Y axis represents *RH*, and color represents the value of the $f(RH)_{LR}$. (**a**–**c**) represent the EXT cases where the fractions of EC are 10%, 20% and 30%, respectively. (**d**–**f**) represent the CS cases where the fractions of EC are 10%, 20% and 30%, respectively. (**g**–**i**) represent the INT cases where the fractions of EC are 10%, 20% and 30%, respectively.

The *LR* value increased with elevated κ and *RH* when the f_{EC} values were 10, 20, and 30% under EXT. Only the non-EC components, which can grow under wet conditions, were considered to be hygroscopic. The extinction and backscattering were exponentially enhanced owing to the growth of non-EC components. The *LR* increased up to 1.8 times when the *RH* ranged from 40% to 100% under the same κ and the f_{EC} value was from 10% to 20%. Nevertheless, the *LR* first decreased and then increased when the f_{EC} value was 30%.

To study the variation of optical parameters due to the hygroscopic growth of aerosol particles, the hygroscopic enhancement factor of the extinction coefficient $f(RH)_{ep}$ and backscattering coefficient $f(RH)_{bac}$ were introduced in Equations (19) and (20), which is the ratio of the optical parameters in the wet state to those in the dry state. The changes in these two optical parameters were studied by defining κ as its median value of 0.25 and with *RH* ranging from 50% to 100%. The results are shown in Figure 9.

$$f(RH)_{ep} = \frac{\alpha_{\mathrm{wet}}}{\alpha_{\mathrm{dry}}} \tag{19}$$

$$f(RH)_{bac} = \frac{\beta_{\mathrm{wet}}}{\beta_{\mathrm{dry}}} \tag{20}$$

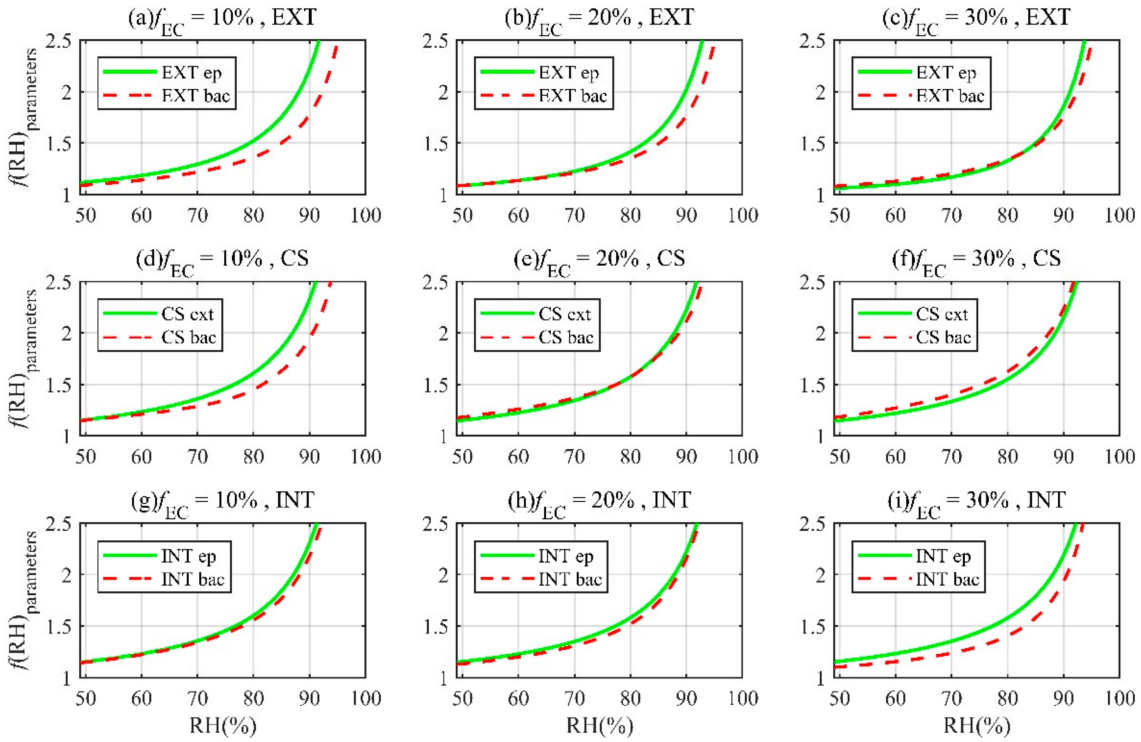

Figure 9. Hygroscopic enhancement factor diagram of optical parameters; the abscissa and ordinate represent the relative humidity and hygroscopic enhancement factor of optical parameters, respectively. (**a**–**c**) represent the EXT cases where the fractions of EC are 10%, 20% and 30%, respectively. (**d**–**f**) represent the CS cases where the fractions of EC are 10%, 20% and 30%, respectively. (**g**–**i**) represent the INT cases where the fractions of EC are 10%, 20% and 30%, respectively.

As is shown in Figure 9, both the extinction and backscattering of aerosols increased with elevated *RH*, while the f_{EC} values were 10%, 20%, and 30%, respectively, which is consistent with the results of other studies [31,33]. Figure 9 shows that the *LR* value depends on the growth rate of extinction and backscattering. For EXT, the growth rate of the extinction was faster than that of the backscattering when the f_{EC} value was 10–20%, leading to a larger *LR*. When the f_{EC} value was 30%, the growth rate of the extinction was slower than that of the backscattering at an *RH* below 80%; thus, the growth rate of the *LR* was slow. When the *RH* exceeded 80%, the growth rate of the extinction exceeded that of the backscattering and the *LR* increased. The *LR* depended primarily on the variation in the particle size distribution caused by the growth of non-EC particles under EXT.

For the CS and INT, the *LR* also increased with κ and *RH* when the f_{EC} value was 10%, which was consistent with the growth rate of the extinction and backscattering shown in Figure 9b,c. When the f_{EC} was 20–30%, the *LR* first decreased with *RH* and then increased under CS, whose change rule was the opposite to that under INT. For CS, the extinction growth rate was slightly lower than that of backscattering at low *RH* values, which leads the *LR* to decrease under low *RH* values. The growth rate of extinction finally matches the growth rate of backscattering when the *RH* value was higher than 90%, therefore the *LR* increases when *RH* is high. However, for INT, the growth rate of extinction was always higher than that of backscattering at low *RH*. The variation in extinction and backscattering increased with increasing *RH* up to 70% and then decreased; thus, the *LR* increased and then decreased with the *RH*. For CS and INT, the *LR* was affected by the change in the particle diameter caused by the hygroscopic growth of non-EC components. All particles contained EC and altered the aerosol absorption during the hygroscopic process for CS and INT, which differed from EXT. On the one hand, the increase in particle thickness or non-EC components enhances the 'lensing effect' and increases light absorption. Conversely, the increase in water accompanied by a change in the complex refraction index will partly lead

to a decrease in the light absorption capacity owing to the growth of hygroscopic particles. Previous studies also showed the optical properties of aerosols and their dependence on humidity. Zieger et al. [57] and Liu et al. [33] have studied the relationship between optical properties and *RH* via experimental and Mie models. Their results showed that the extinction coefficient, scattering coefficient, and backscattering coefficient increase with the increase in *RH*. Ackermann [34] highlighted that the dependence of lidar ratio of different kinds of aerosols on *RH* is different. When *RH* increases, the *LR* of marine aerosol increases first and then decreases at all wavelengths, while that of continental aerosol in 532 nm wavelength increases monotonically with *RH*. Zhao et al. [19] proved that there is a positive correlation between *LR* and *RH*, and he also introduced a scheme of *LR* enhancement factor parameterization. However, their studies did not consider the characteristics of *LR* in different mixing states and different EC fractions. This study analyzes the impact of various factors on the *LR* of aerosols. Overall, the *LR* was comprehensively influenced by the particle effective radius, EC volume fraction, 'lensing effect', and aerosol complex refraction index for CS and INT. It is necessary to consider the impact of the mixing state, EC volume fraction, and aerosol hygroscopicity on the *LR*, as well as the application of *LR* in the retrieval of lidar.

4. Conclusions

A simulation of optical parameters was conducted in this study to investigate the impact factors of the lidar ratio (*LR*) using a three-component optical aerosol assumption based on the Mie model. The impact factors of the *LR* were analyzed, including the aerosol particle number size distribution (PNSD), volume fraction of EC, mixing state, and hygroscopicity of aerosols.

The *LR* of aerosol particles is positively correlated with the overall particle size within a certain scale range of particle size, which is consistent with the conclusion of single particle optical properties obtained by the Mie model. In a certain scale range of particle size, the proportion of backscatter in the entire extinction decreases with an increase in particle size, which leads to an increase in the *LR*.

The *LR* of aerosols was positively correlated with the volume fraction of the EC. The increase in f_{EC} significantly increased the proportion of light absorption, which led to a decrease in the overall scattering and an increase in the *LR*. The *LR* for CS and INT was affected by the 'lensing effect', which increased the proportion of particle light-absorption and reduced the particle scattering, leading to an eventual increase in the *LR*.

The influence of hygroscopicity on the *LR* is dominated by the relative growth rate of the enhancement factor of aerosol extinction and backscattering. The *LR* in EXT is positively correlated with hygroscopic parameters, which is attributed to an increase in particle size caused by the hygroscopic growth. While for the core-shell mixing state and homogeneously mixing state, the *LR* is not only affected by the particle diameter change in the particle hygroscopic growth process but also influenced by the 'lensing effect', which needs further study in the future.

The findings in this study could theoretically be used to establish a scheme of parameterization for *LR*. The *LR* at the target location can be determined quantitatively by real-time measured PNSD, humidity, single hygroscopicity parameters, EC fraction, and mixing state. We believe that the completeness of these parameters will contribute to a more accurate correction of the *LR*. If the data of some parameters cannot be obtained in real-time observation, we suggest to select the appropriate values of the parameters from long-term measurement.

Supplementary Materials: The following supporting information can be downloaded at: https://www.mdpi.com/article/10.3390/rs14071554/s1, Figure S1: PNSD of each region; Figure S2: Statistical chart of the frequency of hygroscopic parameters κ in China; Figure S3: Calculated optical efficiencies of the median PNSD [58].

Author Contributions: Conceptualization, Z.Z. and B.W.; methodology, Z.Z. and L.L.; validation, Z.Z., L.L. and B.W.; formal analysis, Z.Z. and L.L.; investigation, Y.W. and C.L.; resources, B.W.; data curation, Y.W.; writing—original draft preparation, Z.Z. and L.L.; writing—review and editing, B.W., H.T., C.L. and P.C.; project administration, B.W.; funding acquisition, B.W., H.T. and L.L. All authors have read and agreed to the published version of the manuscript.

Funding: This research was funded by the National Natural Science Foundation of China (grant numbers 41775015, 41630422, and 42105092); Guangdong Major Project of Basic and Applied Basic Research (grant number 2020B0301030004); Guangdong Province Key Laboratory for Climate Change and Natural Disaster Studies (grant number 2020B1212060025); Guangdong Basic and Applied Basic Research Foundation (grant number 2019A1515110791); Science and Technology Innovation Team Plan of Guangdong Meteorological Bureau (grant number GRMCTD202003); and Science and Technology Research Project of Guangdong Meteorological Bureau (grant number GRMC2018M07).

Institutional Review Board Statement: Not applicable.

Informed Consent Statement: Not applicable.

Data Availability Statement: Not applicable.

Conflicts of Interest: The authors declare no conflict of interest.

References

1. Ramanathan, V.; Crutzen, P.J.; Kiehl, J.T.; Rosenfeld, D. Aerosols, climate, and the hydrological cycle. *Science* **2001**, *294*, 2119–2124. [CrossRef] [PubMed]
2. Twomey, S. Pollution and the planetary albedo. *Atmos. Environ.* **1974**, *8*, 1251–1256. [CrossRef]
3. Albrecht, B.A. Aerosols, cloud microphysics, and fractional cloudiness. *Science* **1989**, *245*, 1227–1230. [CrossRef] [PubMed]
4. Fernald, F.G.; Herman, B.M.; Reagan, J.A. Determination of aerosol height distributions by lidar. *J. Appl. Meteorol.* **1972**, *11*, 482–489. [CrossRef]
5. Fernald, F.G. Analysis of atmospheric lidar observations: Some comments. *Appl. Opt.* **1984**, *23*, 652. [CrossRef] [PubMed]
6. Liu, Z.; Sugimoto, N.; Murayama, T. Extinction-to-backscatter ratio of Asian dust observed with high-spectral-resolution lidar and Raman lidar. *Appl. Opt.* **2002**, *41*, 2760–2767. [CrossRef]
7. Su, J.; Liu, Z.; Wu, Y.; McCormick, M.P.; Lei, L. Retrieval of multi-wavelength aerosol lidar ratio profiles using Raman scattering and Mie backscattering signals. *Atmos. Environ.* **2013**, *79*, 36–40. [CrossRef]
8. Pappalardo, G.; Amodeo, A.; Pandolfi, M.; Wandinger, U.; Ansmann, A.; Bösenberg, J.; Matthias, V.; Amiridis, V.; De Tomasi, F.; Frioud, M.; et al. Aerosol lidar intercomparison in the framework of the EARLINET project. 3. Raman lidar algorithm for aerosol extinction, backscatter, and lidar ratio. *Appl. Opt.* **2004**, *43*, 5370–5385. [CrossRef]
9. Sroga, J.T.; Eloranta, E.W.; Shipley, S.T.; Roesler, F.L.; Tryon, P.J. High spectral resolution lidar to measure optical scattering properties of atmospheric aerosols. 2: Calibration and data analysis. *Appl. Opt.* **1983**, *22*, 3725–3732. [CrossRef]
10. Hair, J.W.; Hostetler, C.A.; Cook, A.L.; Harper, D.B.; Ferrare, R.A.; Mack, T.L.; Welch, W.; Izquierdo, L.R.; Hovis, F.E. Airborne high spectral resolution lidar for profiling aerosol optical properties. *Appl. Opt.* **2008**, *47*, 6734–6752. [CrossRef]
11. Lopes, F.; Landulfo, E.; Vaughan, M. Assessment of the CALIPSO Lidar 532-nm version 3 lidar ratio models using a ground-based lidar and AERONET sun photometers in Brazil. *Atmos. Meas. Tech. Discuss.* **2013**, *6*, 1143–1199.
12. Chaikovsky, A.; Dubovik, O.; Holben, B.; Bril, A.; Goloub, P.; Tanré, D.; Pappalardo, G.; Wandinger, U.; Chaikovskaya, L.; Denisov, S.; et al. Lidar-Radiometer Inversion Code (LIRIC) for the retrieval of vertical aerosol properties from combined lidar/radiometer data: Development and distribution in EARLINET. *Atmos. Meas. Tech.* **2016**, *9*, 1181–1205. [CrossRef]
13. He, Q.S.; Li, C.C.; Mao, J.T.; Lau, A.K.H.; Li, P.R. A study on the aerosol extinction-to-backscatter ratio with combination of micro-pulse LIDAR and MODIS over Hong Kong. *Atmos. Chem. Phys.* **2006**, *6*, 3243–3256. [CrossRef]
14. Zhao, H.; Mao, J.; Zhou, C.; Gong, X. A method of determining multi-wavelength lidar ratios combining aerodynamic particle sizer spectrometer and sun-photometer. *J. Quant. Spectrosc. Radiat. Transf.* **2018**, *217*, 224–228. [CrossRef]
15. Schuster, G.L.; Vaughan, M.; MacDonnell, D.; Su, W.; Winker, D.; Dubovik, O.; Lapyonok, T.; Trepte, C. Comparison of CALIPSO aerosol optical depth retrievals to AERONET measurements, and a climatology for the lidar ratio of dust. *Atmos. Chem. Phys.* **2012**, *12*, 7431–7452. [CrossRef]
16. Shin, S.-K.; Tesche, M.; Müller, D.; Noh, Y. Technical note: Absorption aerosol optical depth components from AERONET observations of mixed dust plumes. *Atmos. Meas. Tech.* **2019**, *12*, 607–618. [CrossRef]
17. Kim, M.H.; Omar, A.H.; Tackett, J.L.; Vaughan, M.A.; Winker, D.M.; Trepte, C.R.; Hu, Y.; Liu, Z.; Poole, L.R.; Pitts, M.C.; et al. The CALIPSO Version 4 Automated Aerosol Classification and Lidar Ratio Selection Algorithm. *Atmos. Meas. Tech.* **2018**, *11*, 6107–6135. [CrossRef]
18. Shimizu, A.; Sugimoto, N.; Matsui, I.; Mori, I.; Nishikawa, M.; Kido, M. Relationship between lidar-derived dust extinction coefficients and mass concentrations in Japan. *SOLA* **2011**, *7A*, 1–4. [CrossRef]

19. Zhao, G.; Zhao, C.; Kuang, Y.; Tao, J.; Tan, W.; Bian, Y.; Li, J.; Li, C. Impact of aerosol hygroscopic growth on retrieving aerosol extinction coefficient profiles from elastic-backscatter lidar signals. *Atmos. Chem. Phys.* **2017**, *17*, 12133–12143. [CrossRef]
20. Zhao, H.; Hua, D.; Mao, J.; Zhou, C. Investigate the relationship between multiwavelength lidar ratios and aerosol size distributions using aerodynamic particle sizer spectrometer. *J. Quant. Spectrosc. Radiat. Transf.* **2017**, *188*, 12–19. [CrossRef]
21. Song, Y.; Zhang, B.; Shi, G.; Li, S.; Di, H.; Yan, Q.; Hua, D. Correlation between the lidar ratio and the Ångström exponent of various aerosol types. *Particuology* **2018**, *40*, 62–69. [CrossRef]
22. Jacobson, M.Z. Strong radiative heating due to the mixing state of black carbon in atmospheric aerosols. *Nature* **2001**, *409*, 695–697. [CrossRef] [PubMed]
23. Bond, T.C.; Bergstrom, R.W. Light absorption by carbonaceous particles: An investigative review. *Aerosol Sci. Technol.* **2006**, *40*, 27–67. [CrossRef]
24. Myhre, G.; Samset, B.H.; Schulz, M.; Balkanski, Y.; Bauer, S.; Berntsen, T.K.; Bian, H.; Bellouin, N.; Chin, M.; Diehl, T.; et al. Radiative forcing of the direct aerosol effect from AeroCom Phase II simulations. *Atmos. Chem. Phys.* **2013**, *13*, 1853–1877. [CrossRef]
25. Heintzenberg, J. Particle size distribution from scattering measurements of nonspherical particles via Mie-theory. *Contrib. Atmos. Phys./Beitraege Phys. Atmos.* **1978**, *51*, 91–99.
26. Cappa, C.D.; Onasch, T.B.; Massoli, P.; Worsnop, D.R.; Bates, T.S.; Cross, E.S.; Davidovits, P.; Hakala, J.; Hayden, K.L.; Jobson, B.T.; et al. Radiative absorption enhancements due to the mixing state of atmospheric black carbon. *Science* **2012**, *337*, 1078–1081. [CrossRef]
27. Bond, T.C.; Doherty, S.J.; Fahey, D.W.; Forster, P.M.; Berntsen, T.; DeAngelo, B.J.; Flanner, M.G.; Ghan, S.; Kärcher, B.; Koch, D.; et al. Bounding the role of black carbon in the climate system: A scientific assessment. *J. Geophys. Res. Atmos.* **2013**, *118*, 5380–5552. [CrossRef]
28. Ma, N.; Zhao, C.S.; Müller, T.; Cheng, Y.F.; Liu, P.F.; Deng, Z.Z.; Xu, W.Y.; Ran, L.; Nekat, B.; van Pinxteren, D.; et al. A new method to determine the mixing state of light absorbing carbonaceous using the measured aerosol optical properties and number size distributions. *Atmos. Chem. Phys.* **2012**, *12*, 2381–2397. [CrossRef]
29. Tan, H.; Liu, L.; Fan, S.; Li, F.; Yin, Y.; Cai, M.; Chan, P.W. Aerosol optical properties and mixing state of black carbon in the Pearl River Delta, China. *Atmos. Environ.* **2016**, *131*, 196–208. [CrossRef]
30. Liu, D.; Allan, J.D.; Young, D.E.; Coe, H.; Beddows, D.; Fleming, Z.L.; Flynn, M.J.; Gallagher, M.W.; Harrison, R.M.; Lee, J.; et al. Size distribution, mixing state and source apportionment of black carbon aerosol in London during wintertime. *Atmos. Chem. Phys.* **2014**, *14*, 10061–10084. [CrossRef]
31. Adam, M.; Putaud, J.P.; Martins Dos Santos, S.; Dell'Acqua, A.; Gruening, C. Aerosol hygroscopicity at a regional background site (Ispra) in Northern Italy. *Atmos. Chem. Phys.* **2012**, *12*, 5703–5717. [CrossRef]
32. Deng, H.; Tan, H.; Li, F.; Cai, M.; Chan, P.W.; Xu, H.; Huang, X.; Wu, D. Impact of relative humidity on visibility degradation during a haze event: A case study. *Sci. Total Environ.* **2016**, 1149–1158. [CrossRef] [PubMed]
33. Liu, L.; Tan, H.; Fan, S.; Cai, M.; Xu, H.; Li, F.; Chan, P. Influence of aerosol hygroscopicity and mixing state on aerosol optical properties in the Pearl River Delta region, China. *Sci. Total Environ.* **2018**, *627*, 1560–1571. [CrossRef] [PubMed]
34. Ackermann, J. The extinction-to-backscatter ratio of tropospheric aerosol: A numerical study. *J. Atmos. Ocean. Technol.* **1998**, *15*, 1043–1050. [CrossRef]
35. Ferrare, R.A.; Melfi, S.H.; Whiteman, D.N.; Evans, K.D.; Poellot, M.; Kaufman, Y.J. Raman lidar measurements of aerosol extinction and backscattering: 2. Derivation of aerosol real refractive index, single-scattering albedo, and humidification factor using Raman lidar and aircraft size distribution measurements. *J. Geophys. Res. Atmos.* **1998**, *103*, 19673–19689. [CrossRef]
36. Kuang, Y.; Zhao, C.S.; Tao, J.C.; Bian, Y.X.; Ma, N. Impact of aerosol hygroscopic growth on the direct aerosol radiative effect in summer on North China Plain. *Atmos. Environ.* **2016**, *147*, 224–233. [CrossRef]
37. Müller, D.; Ansmann, A.; Mattis, I.; Tesche, M.; Wandinger, U.; Althausen, D.; Pisani, G. Aerosol-type-dependent lidar ratios observed with Raman lidar. *J. Geophys. Res.* **2007**, *112*, D16202. [CrossRef]
38. Kim, M.-H.; Kim, S.-W.; Omar, A.H. Dust Lidar Ratios Retrieved from the CALIOP Measurements Using the MODIS AOD as a Constraint. *Remote Sens.* **2020**, *12*, 251. [CrossRef]
39. Cheng, Y.F.; Wiedensohler, A.; Eichler, H.; Su, H.; Gnauk, T.; Brüggemann, E.; Herrmann, H.; Heintzenberg, J.; Slanina, J.; Tuch, T. Aerosol optical properties and related chemical apportionment at Xinken in Pearl River Delta of China. *Atmos. Environ.* **2008**, *42*, 6351–6372. [CrossRef]
40. Ackerman, T.P.; Toon, O.B. Absorption of visible radiation in atmosphere containing mixtures of absorbing and nonabsorbing particles. *Appl. Opt.* **1981**, *20*, 3661–3667. [CrossRef]
41. Hasan, H.; Dzubay, T.G. Apportioning light extinction coefficients to chemical species in atmospheric aerosol. *Atmos. Environ.* **1983**, *17*, 1573–1581. [CrossRef]
42. Ouimette, J.R.; Flagan, R.C. The extinction coefficient of multicomponent aerosols. *Atmos. Environ.* **1982**, *16*, 2405–2419. [CrossRef]
43. Steinfeld, J.I. Atmospheric chemistry and physics: From air pollution to climate change. *Environ. Sci. Policy Sustain. Dev.* **1998**, *40*, 26. [CrossRef]
44. Sloane, C.S. Optical properties of aerosols of mixed composition. *Atmos. Environ.* **1984**, *18*, 871–878. [CrossRef]
45. Tang, I.N.; Munkelwitz, H.R. Water activities, densities, and refractive indices of aqueous sulfates and sodium nitrate droplets of atmospheric importance. *J. Geophys. Res.* **1994**, *99*, 18801–18808. [CrossRef]

46. Lesins, G.; Chylek, P.; Lohmann, U. A study of internal and external mixing scenarios and its effect on aerosol optical properties and direct radiative forcing. *J. Geophys. Res. Atmos. AAC* **2002**, *107*, AAC 5-1–AAC 5-12. [CrossRef]
47. Köhler, H. The nucleus in and the growth of hygroscopic droplets. *Trans. Faraday Soc.* **1936**, *32*, 1152–1161. [CrossRef]
48. Peng, C.; Wang, Y.; Wu, Z.; Chen, L.; Huang, R.-J.; Wang, W.; Wang, Z.; Hu, W.; Zhang, G.; Ge, M.; et al. Tropospheric aerosol hygroscopicity in China. *Atmos. Chem. Phys.* **2020**, *20*, 13877–13903. [CrossRef]
49. Brock, C.A.; Wagner, N.L.; Anderson, B.E.; Attwood, A.R.; Beyersdorf, A.; Campuzano-Jost, P.; Carlton, A.G.; Day, D.A.; Diskin, G.S.; Gordon, T.D.; et al. Aerosol optical properties in the southeastern United States in summer—Part_1: Hygroscopic growth. *Atmos. Chem. Phys.* **2016**, *16*, 4987–5007. [CrossRef]
50. Wu, T.; Boor, B.E. Urban aerosol size distributions: A global perspective. *Atmos. Chem. Phys.* **2021**, *21*, 8883–8914. [CrossRef]
51. Shin, S.-K.; Tesche, M.; Kim, K.; Kezoudi, M.; Tatarov, B.; Müller, D.; Noh, Y. On the spectral depolarisation and lidar ratio of mineral dust provided in the AERONET version 3 inversion product. *Atmos. Chem. Phys.* **2018**, *18*, 12735–12746. [CrossRef]
52. Yang, F.; Tan, J.; Zhao, Q.; Du, Z.; He, K.; Ma, Y.; Duan, F.; Chen, G.; Zhao, Q. Characteristics of $PM_{2.5}$ speciation in representative megacities and across China. *Atmos. Chem. Phys.* **2011**, *11*, 5207–5219. [CrossRef]
53. Chan, C.K.; Yao, X. Air pollution in mega cities in China. *Atmos. Environ.* **2008**, *42*, 1–42. [CrossRef]
54. Zhang, Q.; Jimenez, J.L.; Canagaratna, M.R.; Allan, J.D.; Coe, H.; Ulbrich, I.; Alfarra, M.R.; Takami, A.; Middlebrook, A.M.; Sun, Y.L.; et al. Ubiquity and dominance of oxygenated species in organic aerosols in anthropogenically-influenced Northern Hemisphere midlatitudes. *Geophys. Res. Lett.* **2007**, *34*, L13801. [CrossRef]
55. Cao, G.; Zhang, X.; Zheng, F. Inventory of black carbon and organic carbon emissions from China. *Atmos. Environ.* **2006**, *40*, 6516–6527. [CrossRef]
56. Hansen, J.E.; Travis, L.D. Light scattering in planetary atmospheres. *Space Sci. Rev.* **1974**, *16*, 527–610. [CrossRef]
57. Zieger, P.; Fierz-Schmidhauser, R.; Weingartner, E.; Baltensperger, U. Effects of relative humidity on aerosol light scattering: Results from different European sites. *Atmos. Chem. Phys.* **2013**, *13*, 10609–10631. [CrossRef]
58. Hussein, T.; Dal Maso, M.; Petaja, T.; Koponen, I.K.; Paatero, P.; Aalto, P.P.; Hameri, K.; Kulmala, M. Evaluation of an automatic algorithm for fitting the particle number size distributions. *Boreal Environ. Res.* **2005**, *10*, 337.